

# The Galactic Chemical Evolution of Carbon: Implications for Stellar Nucleosynthesis

Daniel A. Boyea,<sup>1\*</sup> James W. Johnson,<sup>1</sup> Third Author<sup>2,3</sup> and Others<sup>1,3</sup>

<sup>1</sup>*Department of Astronomy, the Ohio State University, 191 W. Woodruff, Columbus, OH 43210, USA*

Accepted XXX. Received YYY; in original form ZZZ

## ABSTRACT

C is an important element across astronomy; however, its origin remains poorly understood. We aim to constrain the stellar yields of C through multi-zone Galactic chemical evolution models by comparing predictions with APOGEE subgiants abundances. We find that  $[C/Mg]$ - $[Mg/Fe]$  is an empirical estimate of the delayed C sources, enabling us to estimate that AGB stars and CCSNe produce about 20% and 80% of C, respectively. The  $[C/Mg]$ - $[Mg/H]$  trend instead represents the equilibrium abundances of C and Mg. We use the  $[C/Mg]$ - $[Mg/H]$  trend to estimate the CCSNe C/Mg yield, determining that  $y_C^{cc}/y_{Mg}^{cc} = \text{EQUATION}$  when including AGB C. Our models are relatively independent of uniform scaling of yields and outflows, and alternate star formation histories. However, the stars which contribute to AGB C production and the SNe Ia delay time distribution of Fe contribute uncertainties to our conclusions. While reliable gas-phase and low-metallicity measurements of C are challenging, we find that our model and a single-zone model with our recommended yields replicate the broad trends of  $[C/Mg]$ - $[Mg/H]$  across different environments and metallicities.

## 1 INTRODUCTION

Carbon is a distinctive and well-studied element in astronomy. Formed in the cores of stars during He fusion, C is the lightest directly synthesized element after He, one of the only light elements formed in low-mass stars, and one of the most abundant metals (e.g. Johnson 2019; Karakas & Lattanzio 2014).<sup>1</sup> C structurally changes the environments it pollutes – regulating stellar evolution, facilitating the formation of stars and planets, and forming the basis of earthly life. As such, understanding the origin of C has wide ranging implications. While we know both lower-intermediate-mass and high-mass stars produce C, the relative importance of each process is still unknown.

We know, from observations of MW stars and (extragalactic) gas, that C/O traces a banana shape in O/H (see Fig. 10 and section 5.6). At the very lowest metallicities, where  $[O/H] \lesssim -2$ ,<sup>2</sup> observations suggest that C/O declines with metallicity. From  $-2 \lesssim [O/H] \lesssim -1$ , C/O is roughly constant with metallicities. And, at higher metallicities  $-1 \lesssim [O/H]$ , C/O increases with increasing metallicity. As our primary observational constraint, we use a sample of subgiant stars from the APOGEE (Majewski et al. 2017) selected by the criteria in Roberts et al. (2023, in prep). According to stellar evolution theory and observations (Gilroy 1989; Korn et al. 2007; Lind et al. 2008; Souto et al. 2018, 2019), these stars have not yet experienced first dredge up<sup>3</sup> yet have well-mixed envelopes. So, subgiant sur-

face abundances most accurately represent their birth composition. In contrast, evolved RGB stars require modelling-dependent corrections to recover birth C abundances (e.g. Vincenzo et al. 2021). Fig. 1 shows the subgiant sample plotted in  $[C/Mg]$ - $[Mg/H]$  and  $[C/Mg]$ - $[Mg/Fe]$ .  $[C/Mg]$  increases with metallicity, and  $[C/Mg]$  decreases with  $[Mg/Fe]$  at fixed  $[Mg/H]$ . Using the subgiant abundance trends, we will develop a model of the enrichment sources and evolution of C.

Galactic chemical evolution (GCE) is a powerful tool, capable of uncovering the origins of the elements. Each enrichment process has characteristic chemical signatures and timescales, enabling us to reconstruct chemical histories. Many previous works have used GCE in attempt to understand C abundances, whether through using theoretical stellar models (Dearborn et al. 1978; Prantzos et al. 2018; Chiappini et al. 2003) or understanding observation (Tinsley 1979; Henry et al. 2000; Bensby & Feltzing 2006; Rybizki et al. 2017; Berg et al. 2019; Kobayashi et al. 2020; See also review in Romano 2022). Every study agrees that C is produced by a combination of high-mass and lower-intermediate mass stars, different studies disagree on which process is dominant. For example CITES conclude high-mass stars dominate whereas CITES conclude lower-intermediate mass stars contribute the majority of C. C is also generally understood to have strong metallicity dependent CCSNe enrichment.

One of the primary uncertainties of GCE models are nucleosynthetic yields. Yield predictions – the amounts of each chemical element stars produce – are shaped by poorly understood processes, including mass loss, nuclear reaction rates, rotational mixing, convection, and explosibility (Romano et al. 2010; Karakas & Lattanzio 2014; Ventura et al. 2013; Limongi & Chieffi 2018; Griffith et al. 2021). To better understand where C comes from and how it evolves, our aim is to combine APOGEE observations and multi-zone models to develop observationally-consistent yields. Johnson et al. (2023) examined similar GCE models of N (which is closely related to C), finding that trends in N and O are explained by the metallicity dependence of N/O yields. Johnson et al. (2023) determine that AGB N

<sup>1</sup> By metallicity, we mean the (mass) fraction of any element which is not H or He, denoted by Z. For the sun, we take  $Z_\odot = 0.014$ .

<sup>2</sup> In this paper, we use the standard notation for chemical abundances.  $[A/B] = \log_{10}(A/B) - \log_{10}(A_\odot/B_\odot)$ , i.e.  $[A/B]$  is the logarithm of the ratio between A and B, scaled such that  $[A/B] = 0$  for the sun. Solar abundances are as measured in Asplund et al. (2009).

<sup>3</sup> First dredge up is when material from CNO processed core is mixed with the (convective) stellar envelope during the ascent onto the RGB. As a result, C is decreased and N is increased depending on the strength of this process and the envelope mass.

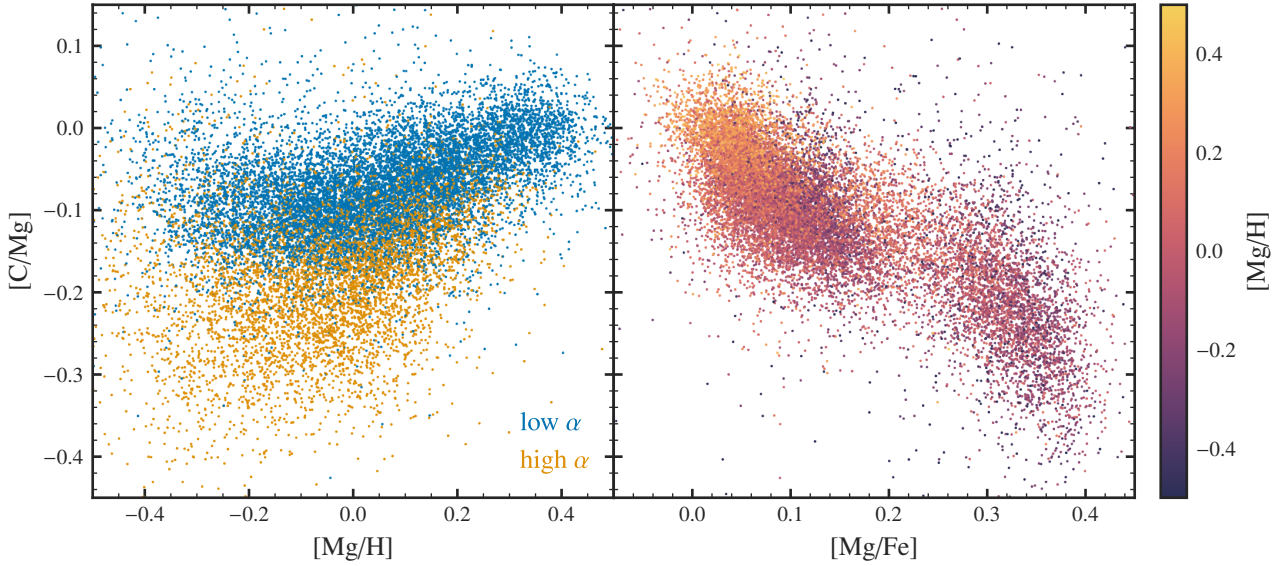


**Figure 1.** The  $[C/Mg]$  ratio against  $[Mg/H]$  (top) and  $[Mg/Fe]$  (bottom) for the Roberts et al. (2023, in prep.) sample of APOGEE subgiants. On the top, we plot high and low- $\alpha$  stars in blue and orange, using the separation defined in Equation 12 (the high and low- $\alpha$  stars are named for their high or low  $\alpha$ -element to Fe ratios, or in this case,  $Mg/Fe$ ). On the bottom, we colour-code stars according to their  $[Mg/H]$  abundance.

abundances roughly depend linearly on metallicity (i.e.  $y_N/y_O \propto Z$ ). Here, we extend their models to C, deriving similar constraints on C/Mg yields. We assess which yield prescriptions reproduce Galactic abundance trends while investigating the impact of GCE model assumptions, such as the star formation history (SFH) and outflow mass loading.

## 2 NUCLEOSYNTHESIS

We adapt the yield choices of elements besides C from Johnson et al. (2021, 2023). Table 1 contains our fiducial yields. Following Johnson et al. (2021, 2023), we also take the SNe Ia delay time distribution to be a  $t^{-1.1}$  power-law with a minimum delay time of 140 Myr, as suggested by the observations of Maoz et al. (2012).

Yields – the amounts of each chemical element stars synthesise – are central to studies of galactic chemical evolution (GCE). In this section, we compare literature yield predictions and discuss our fiducial yield choices. We focus on three nucleosynthetic pathways: asymptotic giant branch (AGB) stars, core collapse supernovae (CC-SNe), and type Ia supernovae (SNe Ia). C is produced in both AGB and CCSNe stars. We also use Mg and Fe as tracers of CCSNe and SNe Ia enrichment respectively. O and Mg are produced almost entirely from CCSNe with metallicity-independent yields. In contrast, Fe is produced in similar amounts by CCSNe and SNe Ia.

After a single stellar population (SSP)<sup>4</sup> forms, CCSNe are the first chemical enrichers. CCSNe explode within  $\lesssim 40$  Myr, providing light elements (e.g. C, O, and Mg) and heavier elements (Fe and beyond). Next, low-mass stars begin to reach the end of their lives, entering the AGB phase. By shedding their outer layers, AGB stars are important sources of C, N, and neutron capture elements. Finally, white dwarfs explode in SNe Ia, releasing Fe and other iron-peak elements.

To quantify yields, we define the stellar yield to be the fraction of a stars initial mass which is newly synthesized and released as a given element. For an element  $X$  and star with mass  $M$ , the net-fractional stellar yield  $Y$  is

$$Y_X = \Delta Z_X \frac{M_{\text{ejected}}}{M_{\text{birth}}} \quad (1)$$

where  $M_{\text{ejected}}$  and  $M_{\text{birth}}$  are the total ejected mass and the birth mass of the star, and  $\Delta Z_X$  is the change in  $Z_X$  from the birth material to the ejected material of the star.<sup>5</sup> For example, a  $1 M_{\odot}$  star with  $Y_C = 10^{-3}$  will add  $10^{-3} M_{\odot}$  of new C to the interstellar medium. Also, note that yields may be negative if the material returned to the interstellar medium has a lower abundance  $Z_X$  than the material the star was formed from. Although per-star yields are necessary to compute AGB star enrichment rates in GCE models, initial-mass-function (IMF) averaged yields are useful in interpreting their predictions. An IMF-averaged yield adds together the yields of stars of each mass, weighted by the fraction of stars of each mass (the IMF). Given the fractional yield  $Y(M, Z)$  as a function of initial stellar mass  $M$  and metallicity  $Z$ , the IMF-averaged yield is given by

$$y_X(Z, t) = \frac{\int_{M_{\min}(t)}^{M_{\max}} Y_X(M, Z) \frac{dN}{dM} M dM}{\int \frac{dN}{dM} M dM} \quad (2)$$

where  $dN/dM$  is the IMF,  $M_{\max} = 100 M_{\odot}$  is the maximum stellar mass, and  $M_{\min}(t)$  is the mass of stars with lifetime  $t$ .<sup>6</sup> To calculate the IMF-averaged net yields, we use the Versatile Integrator for Chemical Evolution code (VICE).<sup>7</sup>

<sup>5</sup>  $Z_X$  represents the mass fraction of element  $X$ .

<sup>6</sup> In our model, the mass-lifetime relation is  $\log \tau_M = 1.02 - 3.57 \log M + 0.90 (\log M)^2$ , where  $\tau_M$  is in Gyr, from Larson 1974. We use  $t_{\text{end}} = 10$  Gyr for total yields when  $t$  is not used.

<sup>7</sup> VICE is available at <https://github.com/giganano/VICE>

<sup>4</sup> SSP: Single stellar population. Technical name for a group of stars born in the same conditions at the same time, i.e. an open cluster.

**Table 1.** Yields for the fiducial model (in units of SSP birth mass). See Section 2.1 for the definition of C11.

Element	$y^{\text{cc}}$	$y^{\text{agb}}$	$y^{\text{ia}}$
C	Eq. 7	$2.3 \times \text{C11}$	0
O	0.015	0	0
Mg	0.00185	0	0
Fe	0.0012	0	0.00214
N	0.00072	$0.0009M\left(\frac{Z}{Z_{\odot}}\right)$	0

## 2.1 Asymptotic Giant Branch Stars

An AGB star is a low-mass ( $\lesssim 8 M_{\odot}$ ) star during its final phase of evolution. Inside an AGB star, an inert CO core is surrounded by thermally-unstable He and H-burning shells below a convective envelope. In an AGB star, two competing processes determine the outcome of C production: *third dredge up* and *hot bottom burning*. Third dredge up accompanies thermal pulses in AGB stars, where material from the CO core is mixed with the envelope, increasing surface C abundances (Karakas & Lattanzio 2014). The C yields of the star are increased as this C-enhanced envelope is released to the interstellar medium. Hot bottom burning is the activation of the CNO cycle<sup>8</sup> at the bottom of the convective envelope when  $T \gtrsim 50$  MK. Because the  $^{14}\text{N}$  proton capture is the slowest component of the CNO cycle, the CNO cycle converts nearly all  $^{12}\text{C}$  into  $^{14}\text{N}$  (Adelberger et al. 2011).

Hot bottom burning and third dredge-up result in mass-dependent C yields. Stars less than  $\sim 2 M_{\odot}$  do not experience third dredge-up. As a result, these stars C abundances are only affected by first dredge-up, resulting in little change to C yields or slight destruction of C. Above  $\sim 2 M_{\odot}$ , third dredge up becomes important, enriching the outer layers with C. AGB stars between 2 and  $5 M_{\odot}$  are the most abundant producers of C. In AGB stars more massive than  $\sim 5 M_{\odot}$ , both hot bottom burning and third dredge up occur; however, hot bottom burning is much more efficient, resulting in significant  $^{12}\text{C}$  destruction.

In this work, we explore four different sets of AGB star yield tables from literature, providing necessary well-sampled grids in mass and metallicity. We refer to the yields from the following studies as the following. For our models to match observations, we find that need to uniformly amplify these yield tables. We use C11 table, amplified by a factor of 2.9, as the fiducial AGB yield. Variations in models are due to different treatments of reaction rates, convection, and mass-loss.

C11: Cristallo et al. (2011, 2015)

K10: Karakas (2010)

V13: Ventura et al. (2013, 2014, 2018, 2020)

K16: Karakas & Lugaro (2016); Karakas et al. (2018)

Fig. 2 compares the stellar AGB C yields for these four models. Most models agree on the qualitative shape of the net fractional AGB C yield. Stellar yields peak between masses of about  $2\text{--}4 M_{\odot}$  and decline as stars become more or less massive. As metallicity increases, the total AGB C yield decreases. The mass of peak C yields also increases slightly with metallicity. Metal poor stars dredge up more material due to the decreased power of the CNO cycle, resulting in

<sup>8</sup> The CNO cycle is a series of proton-capture reactions with CNO elements resulting in energy generation and the creation of an  $\alpha$  particle.  $^{12}\text{C}(p, \gamma)^{13}\text{N}(\beta^+, \nu_e)^{13}\text{C}(p, \gamma)^{14}\text{N}(p, \gamma)^{15}\text{O}(\beta^+, \nu_e)^{15}\text{N}(p, \alpha)^{12}\text{C}$ . There are other less important minor branches of the CNO cycle (Adelberger et al. 2011).

increasing carbon yields with decreasing metallicity (Ventura et al. 2013).

Fig. 3, on the left, shows the total production of C by AGB stars in a SSP at an age  $t$ , i.e.  $Y_{\text{C}}(Z_{\odot}, t)$ . As the mass range  $2 M_{\odot} \lesssim M \lesssim 4 M_{\odot}$  is most important for C production, about half of C production occurs before  $\sim 1$  Gyr, similar to SNe Ia Fe. K10 and K16 weight C production more heavily towards high-mass AGB stars resulting in a faster enrichment delay time, whereas the C11 and V13 models predict a slightly longer timescale of  $\sim 1$  Gyr. In any case, little to no C is produced more than 2 Gyr after a star formation event. Fe production, in contrast, continues steadily for 10 Gyr.

The right panel of Fig. 3 shows IMF-averaged C yields for each AGB model as a function of metallicity. V13 differs in that it shows a non-monotonic metallicity dependence. However, this effect is only for models with  $\log Z/Z_{\odot} \lesssim -1$ . Otherwise, models differ only in their yield normalization and metallicity dependence. All yield models span a range of  $\sim 2$  for a given metallicity. For example, all four models predict  $y_{\text{C}}^{\text{agb}}(Z_{\odot})$  to be between 0.004 and 0.008 at solar metallicity. The models also differ slightly in the strength of metallicity dependence, with about a factor of 3 discrepancy (see Table 2).

## 2.2 Core Collapse Supernovae

Massive stars form  $^{12}\text{C}$  in their cores through the triple- $\alpha$  process.<sup>9</sup> However, only C ejected through supernovae and stellar winds contributes to the yield. While there are many stellar models providing predictions of CCSNe yields, the results of these models are highly uncertain due to the complexity of stellar modeling.

Fig. 4 plots calculations of the IMF-integrated yields, defined with Eq. 2 (computed using VICE’s `vice.yields.ccsne.fractional` function). CCSNe models predict a wide range of C yields, spanning almost a factor of ten. Both the Nomoto et al. (2013) and Limongi & Chieffi (2018) models show positive metallicity dependence. As metallicity increases, stars lose more of their mass to winds. In particular, C enriched envelop material is lost through winds before synthesized into heavier elements, so C yields can be strongly metallicity dependent (VERIFY). Fig. 4 shows the C11 AGB model for comparison on the left. Especially at  $Z \approx Z_{\odot}$ , most CCSNe models dominate AGB C production. Later, we will also show empirically this is the case. The right of Fig. 4 shows the CCSNe  $[\text{C}/\text{Mg}]$  ratio for the different models, defined by

$$[\text{C}/\text{Mg}]^{\text{CC}} = \log_{10} \left( \frac{y_{\text{C}}^{\text{cc}}}{y_{\text{Mg}}^{\text{cc}}} \right) - \log_{10} \left( \frac{Z_{\text{C}, \odot}}{Z_{\text{Mg}, \odot}} \right). \quad (3)$$

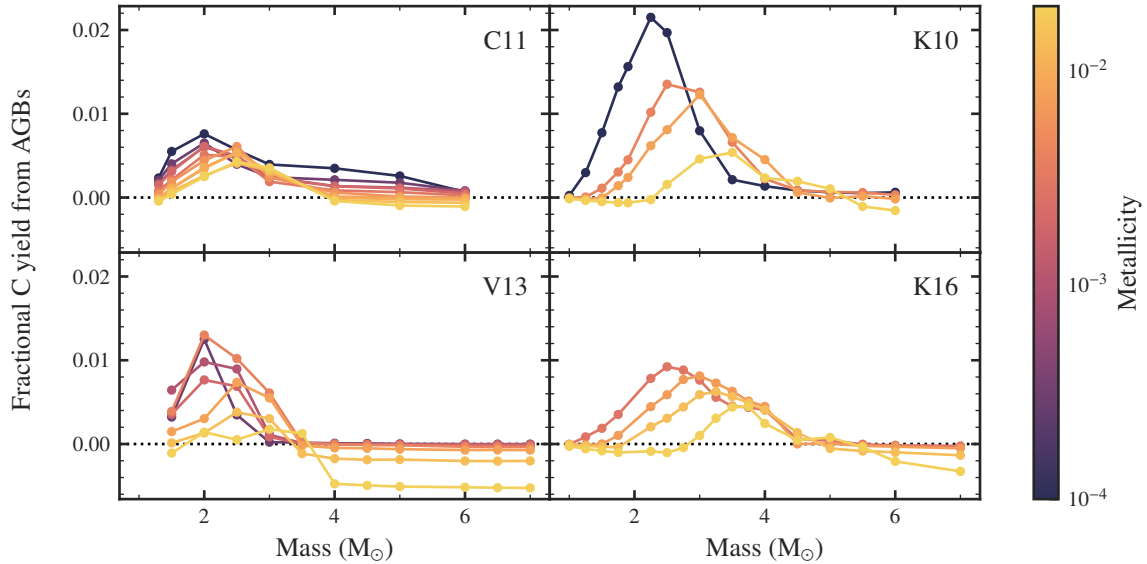
If only CCSNe produced C, then  $[\text{C}/\text{Mg}]^{\text{CC}}$  describes the equilibrium abundance of  $[\text{C}/\text{Mg}]$ . Different CCSNe models also span a large range in  $[\text{C}/\text{Mg}]$ . We chose to instead parameterize  $y_{\text{C}}^{\text{cc}}$  to simplify model inputs, as most CCSNe models fail to achieve near-solar  $[\text{C}/\text{Mg}]$ .

Both rotation and explodability introduce substantial variations. The Limongi & Chieffi (2018) models include rotation, showing that variations in the rotational velocity of the star can dramatically increase the magnitude and metallicity dependence of  $y_{\text{C}}^{\text{cc}}$ . Rotation induces more mixing allowing the CO core to grow larger and contributes to wind losses. As we will later show, CCSNe C production needs to be strongly metallicity-dependent at  $Z/Z_{\odot} \approx 1$ , which is

<sup>9</sup> The 3- $\alpha$  process fuses 3 He nuclei into  $^{12}\text{C}$ .

**Table 2.** For each AGB yield set, the IMF-averaged AGB C yield at solar metallicity  $y_{C,0}^{\text{agb}}$  and the multiplicative factor reaches an AGB contribution of 20%  $\alpha_{\text{agb},20}$ .

AGB table	$y_C^{\text{agb}}(Z_\odot)$	$\zeta^{\text{agb}}(Z_\odot)$	$\alpha_{20}^{\text{agb}}$	masses ( $M_\odot$ )	metallicities
<b>C11</b>	0.00042	-0.0175	2.4	1.3, 1.5, 2, 2.5, 3, 4, 5, 6	0.0001, 0.0003, 0.001, 0.002, 0.003, 0.006, 0.008, 0.01, 0.014, 0.02
<b>K10</b>	0.00064	-0.059	1.6	1, 1.25, 1.5, 1.75, 1.9, 2.25, 2.5, 3, 3.5, 4, 4.5, 5, 5.5, 6	0.0001, 0.004, 0.008, 0.02
<b>V13</b>	0.00022	-0.021	4.5	1.5, 2, 2.5, 3, 3.5, 4, 4.5, 5, 6, 6.5, 7	0.0003, 0.001, 0.002, 0.004, 0.008, 0.014, 0.04
<b>K16</b>	0.0005	-0.029	2.0	1, 1.25, 1.5, 1.75, 2.25, 2.5, 2.75, 3, 3.25, 3.5, 3.75, 4, 4.5, 5, 5.5, 6, 7	0.0003, 0.001, 0.002, 0.004, 0.008, 0.014, 0.04

**Figure 2.** The net fractional AGB C yield plotted as a function of initial stellar mass  $M$  and colour-coded according to metallicity. The black dashed line shows  $Y = 0$  for reference. Each panel represents yields from one of four AGB models: **C11**, **K10**, **V13**, **K16**, and our analytic model (see sections 2.1)

consistent with the Limongi & Chieffi (2018) rapidly rotating models. Assumptions about the explodability landscape affect C and Mg production. As fewer high-mass stars explode, both C and Mg yields decrease, but Mg yields decrease more as more C is lost to winds, so  $[C/Mg]$  increases with decreasing explodability.

O and Mg are both  $\alpha$ -elements, light elements produced in CCSNe through He-nuclei fusion. As we focus on constraining relative yields, we neglect O and Mg yield variations in the main text (excluding the uniform scaling of yields and massloading in Section 5.5). There is substantial variation in predicted Mg yields. Most models predict relatively flat trends metallicity (even with rotation as in Limongi & Chieffi 2018). However, the variation is significant and our adopted  $y_{Mg}^{\text{cc}}$  yield is much higher than most models, but O and Mg yields of CCSNe models do not fully match observations. CCSNe models underpredict  $[Mg/O]$ , and the reason why is unknown (see e.g. Grifith et al. 2021). Here, we assume  $[O/Mg] = 0$ , which nevertheless consistent with APOGEE observations (Weinberg et al. 2019, 2022).

### 2.3 Equilibrium Abundances

Here, we assume a simple *one-zone* chemical evolution model (e.g. Tinsley 1980; Pagel 2009; Matteucci 2021). Galaxies, when moder-

ated by metal-poor gas accretion and feedback-driven outflows, reach a chemical equilibrium. The production of new metals is balanced by losses to new stars and outflows (Larson 1972; Dalcanton 2007; Finlator & Davé 2008; Peeples & Shankar 2011; Lilly et al. 2013). While our galaxy is likely not in perfect equilibrium or described by a single, homogeneous chemical environment, the equilibrium approximation is nevertheless useful in understanding yields and metallicity dependence of solar neighborhood stars (e.g. Johnson et al. 2022, 2023; Weinberg et al. 2017).

Johnson et al. (2023) show that trends in N and O abundance ratios are set by the yield ratio and their metallicity dependences. Here, we find a similar conclusion for C and Mg, where equilibrium C/Mg is given by

$$\frac{Z_C^{\text{eq}}}{Z_{Mg}^{\text{eq}}} = \frac{y_C^{\text{cc}} + y_C^{\text{agb}}}{y_{Mg}}. \quad (4)$$

In Fig. 5, we show the inferred total C yields, based on this equation, and our best fitting linear model. From a linear regression, we

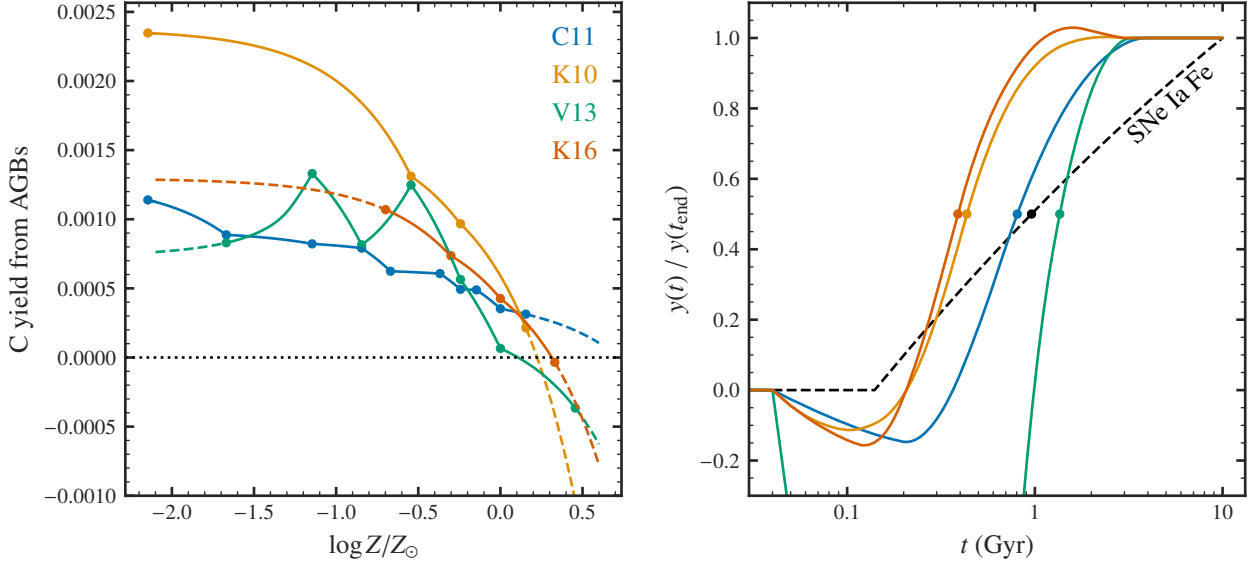


**Figure 3.** C yields from AGB stars as a function of SSP age, as a fraction of the C yield at  $t_{\text{end}} = 10$  Gyr. **Left** The (IMF-weighted) AGB C yield  $y_C^{\text{agb}}$  as a function of metallicity for each of the AGB yield models. ( $y_C^{\text{agb}}$  is the net mass of C produced by AGB stars per unit mass of star formation, after 10 Gyr and assuming a Kroupa 2001 IMF.) **Right** Our four considered AGB yield models at solar metallicity (C11, K10, V13, K16). The dashed red line shows the delay time distribution of type Ia supernovae ( $\propto t^{-1.1}$ ) for comparison, and the minimum of V13 is  $y(t)/y(t_{\text{end}}) = -3.3$ .

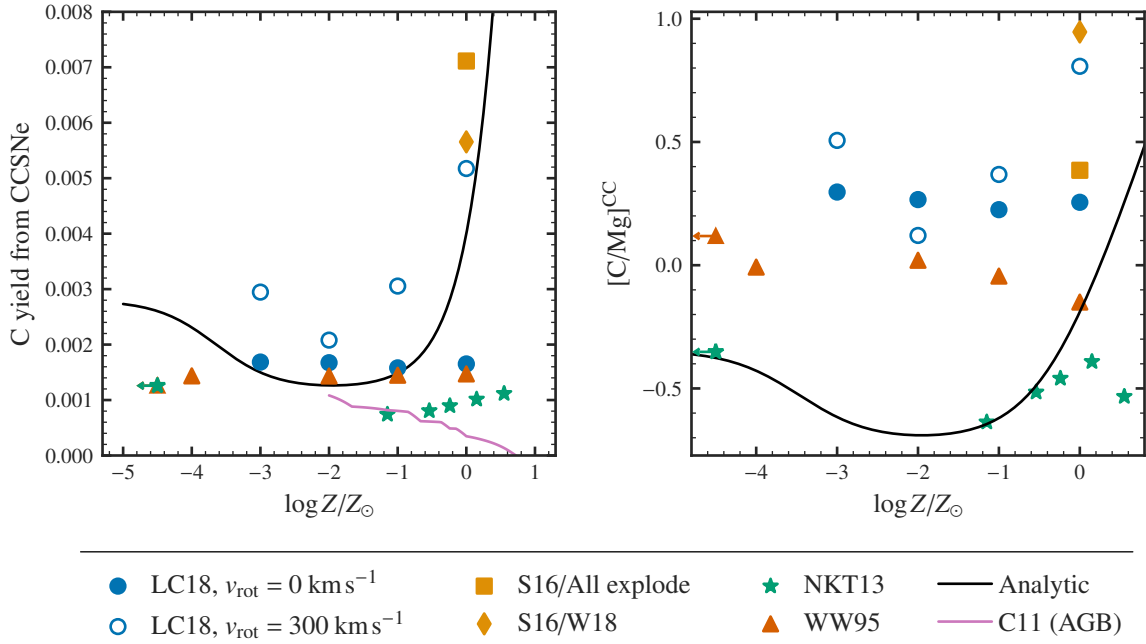


**Figure 4.** C yields from high-mass stars. **Left** The IMF-weighted CCSNe yield of C as a function of metallicity. **Right** The CCSNe  $[\text{C}/\text{Mg}]^{\text{CC}}$  abundance ratio, defined in Eq. 3. The black line is the derived C yield from Section 2.3 and Eq. 7. Yields are shown for tables from Woosley & Weaver (1995, red triangles), Sukhbold et al. (2016, orange squares and diamonds), Nomoto et al. (2013, green stars), and Limongi & Chieffi (2018, blue circles). Sukhbold et al. (2016) report yields for different black hole landscapes, while Limongi & Chieffi (2018) provide yields at different rotational velocities. In the top panel, the pink line denotes  $y_C^{\text{agb}}$  from C11 for comparison. All models include wind yields.



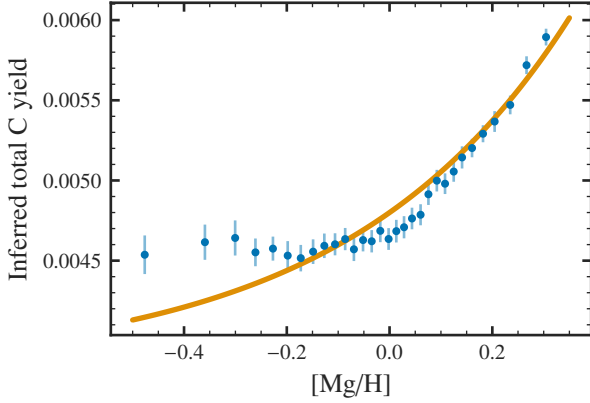


**Figure 5.** Inferred total C yields as a function of metallicity. We assume chemical equilibrium (orange curve, see discussion in Section 2.3). Blue points are the median value of  $y_C^{\text{cc}}$  for each (number) bin in  $[\text{Mg}/\text{H}]$  with uncertainties based on the 16–84 percentile range.

suggest that

$$\frac{y_C(Z)}{y_O} \approx \frac{1}{3} + 4(Z - Z_\odot) \quad (5a)$$

$$\frac{y_C(Z)}{y_{\text{Mg}}} \approx 2.7 + 32(Z - Z_\odot). \quad (5b)$$

These yield ratios results in an equilibrium abundance  $[C/\alpha] = -0.09$ , which is consistent with the subgiant sample and is within  $\sim 20\%$  of the solar C/Mg mixture from Asplund et al. (2009).

Both observational and theoretical uncertainties limit the accuracy of our relative yield predictions. As the metallicity range of our data is small ( $-0.4 \leq [\text{Mg}/\text{H}] \leq 0.4$ ), our model does not extend beyond near-solar metallicities. Additionally, the derived yields will be systematically biased if the galaxy is out of equilibrium, for example, due to a recent starburst (Mor et al. 2019; Isern 2019). As we will discuss in Section 5.5, the normalization of yields and  $\eta$  is degenerate. If we increase yields and  $\eta$  by a similar factor, equilibrium abundances from Eq. 4 would be unchanged, so our model cannot distinguish changes in both yields and outflows.

With the total C yield of Eq. 5 and given an AGB C yield, we can derive an observationally-consistent CCSNe C yield.

$$y_C^{\text{cc}}(Z_\odot) = y_C(Z_\odot) - y_C^{\text{agb}}(Z_\odot) \quad (6a)$$

$$\zeta^{\text{cc}} \equiv \frac{dy_C^{\text{cc}}(Z_\odot)}{dZ} = \frac{dy_C(Z_\odot)}{dZ} - \frac{dy_C^{\text{agb}}(Z_\odot)}{dZ} \quad (6b)$$

This method reduces the number of free parameters of the model and enables all models to match  $[C/\text{Mg}]$ - $[\text{Mg}/\text{H}]$  trends in APOGEE subgiants when considering AGB yields with different metallicity dependences and normalizations. Table 2 contains our adaptive (regression-derived) values of  $\zeta^{\text{agb}}$  and  $y_C^{\text{agb}}(Z_\odot)$ . For example, in our fiducial model,  $y_C^{\text{cc}} = 0.004 + 0.102(Z - Z_\odot)$ . Our full CCSNe C yield model adds a low-metallicity enhancement term, which is insignificant at solar metallicities (e.g. thin disk stars) but enables models in Section 5.6 to match low-metallicity environments. We parameterize low-metallicity enrichment with  $y_l$  and  $Z_l$ , the yield and transition metallicity for enhanced low-metallicity yields. All-together,

$$y_C^{\text{cc}} = y_{C,0}^{\text{cc}} + \zeta^{\text{cc}}(Z - Z_\odot) + \frac{2y_l}{1 + Z/Z_l}. \quad (7)$$

### 3 THE MULTI-ZONE MODEL

Our models extends the Johnson et al. (2021, hereafter J21) Milky Way model, run with the publicly available Versatile Integrator for Chemical Evolution (VICE). This model is described extensively in J21 and concisely summarized in Johnson et al. (2023). Here, we provide a brief overview of the relevant model components. Classical, *one-zone* models of chemical evolution assume instantaneous mixing of metals in the star-forming interstellar medium (e.g. Matteucci 2021). This simple framework is a poor approximation of the Milky Way. The Galaxy evolves *inside-out* – where star formation is higher towards the center and in the early universe (Bird et al. 2013). Additionally, stars can migrate several kpc over their lifetimes, mixing different chemical environments across the galaxy (Bird et al. 2012; Sellwood & Binney 2002). For the rest of this paper, we focus on multi-zone models, which discretize the Galaxy into concentric rings in which stars move between.

Star formation is set separately for each zone. The Galaxy is divided into 200 rings, each 100 pc wide representing a single zone. Each ring (or zone) has a separate stellar population and gas supply. We initially assume an inside-out SFH, where the star formation surface density  $\Sigma_\star$  is given by

$$\dot{\Sigma}_\star \propto \left(1 - e^{-t/\tau_{\text{rise}}}\right) e^{-t/\tau_{\text{sff}}}. \quad (8)$$

$\tau_{\text{rise}} = 2 \text{ Gyr}$  describes when the star formation rate reaches a maximum, and  $\tau_{\text{sff}}$  describes the decay timescale of star formation as a function of radius  $R$ . J21 derives  $\tau_{\text{sff}}(R)$  through analysis of four integral field spectroscopy surveys in Sánchez (2020). At each  $R$ , the SFH is normalized to match the stellar surface density gradient (Bland-Hawthorn & Gerhard 2016) and the total stellar mass reaches  $5.17 \times 10^{10} M_\odot$  (Licquia & Newman 2015). Star formation ends beyond a radius  $R = 15.5 \text{ kpc}$ . The gas inflow is calculated to maintain the SFH for each radius and time, using an extension of a Kennicutt-Schmidt law (Kennicutt 1998),

$$\dot{\Sigma}_\star \propto \begin{cases} \Sigma_{\text{gas}} & 2 \times 10^7 \leq \Sigma_{\text{gas}} \\ (\Sigma_{\text{gas}})^{3.6} & 5 \times 10^6 \leq \Sigma_{\text{gas}} < 2 \times 10^7 \\ (\Sigma_{\text{gas}})^{1.7} & \Sigma_{\text{gas}} < 5 \times 10^6 \end{cases} \quad (9)$$

where  $\Sigma_{\text{gas}}$  is measured in  $M_\odot \text{ kpc}^{-2}$ . The scaling of this relationship varies with time due to the redshift dependence of  $\tau_\star$  in molecular gas observed by Tacconi et al. (2018). We assume a Kroupa (2001) IMF.

To account for radial migration, we use the h277 hydrodynamical simulation results (with simulation parameters as in Bird et al. 2021; see also Christensen et al. 2012; Zolotov et al. 2012; Loebman et al. 2012; Brooks & Zolotov 2014). Each VICE single stellar population (SSP) is matched to an *analog* in H277, chosen to form at a similar time and radius  $R$ . By taking the change in radius  $\Delta R$  of the analogs, the SSPs move to their final radii with a  $\sqrt{\text{time}}$  dependence. The  $\Delta R \propto \sqrt{\text{time}}$  dependence arises when migration proceeds as a consequence of the diffusion of angular momentum (Frankel et al. 2018, 2020). We do not account for radial gas flows. Using the results of a hydrodynamical simulation without modification limits the free parameters in the model; however, we are limited to one dynamical history. We also explore a normal-distribution random walk migration based on Frankel et al. (2018), without noticeable impacts on our results. All models shown here use the h277-based migration. The full impact of the details of a galaxy’s dynamical history on its chemical evolution is still unknown.

As the strength of outflows controls the resulting  $\alpha$ -element abun-

dances, J21 create a metallicity gradient by defining

$$\eta(R) = r - 1 + \frac{y_{\alpha}^{\text{CC}}}{Z_{\alpha,\odot}} 10^{(-0.08 \text{ kpc}^{-1})(R-4 \text{ kpc})+0.3}. \quad (10)$$

This choice of  $\eta(R)$  results in a  $[\alpha/\text{H}]$  gradient consistent with Milky Way observations (e.g. Hayden et al. 2014; Weinberg et al. 2019; Frinchaboy et al. 2013).

#### 4 DATA SELECTION

Subgiants provide the ideal observational constraint to our model. When a star enters the Red Giant Branch (RGB), material from the CNO-processed core is mixed with the envelope in first dredge up, enhancing N and depleting C (Iben 1967; Vincenzo et al. 2021; Karakas & Lattanzio 2014). RGB stars thus require model-dependent corrections to recover surface abundances (e.g. Vincenzo et al. 2021). On the other hand, gravitational settling can affect main sequence stellar abundances (e.g. Souto et al. 2019). Subgiants have well-mixed envelopes, so gravitational settling is not as significant, and subgiants have not yet experienced first dredge up. We use a sample of APOGEE DR17 stars (Majewski et al. 2017) as selected in Roberts et al. (2023, in prep.).

When plotting the data and models, we bin by groups of 500 (or 150) stars in  $[\text{Mg}/\text{H}]$  ( $[\text{Mg}/\text{Fe}]$ ). When plotting  $[\text{C}/\text{Mg}]$ - $[\text{Mg}/\text{H}]$ , we select only the low- $\alpha$  sequence. For  $[\text{C}/\text{Mg}]$ - $[\text{Mg}/\text{Fe}]$ , we instead select stars with  $-0.15 \leq [\text{Mg}/\text{H}] \leq -0.05$ . To create a sample with similar characteristics of the subgiant observations, we sample 12,000 stars from the simulations such that the cumulative distribution function of stars in  $R_{\text{gal}}$  is the same for the subgiants and our comparison sample.

As the primary observational constraint, we use the criteria outlined in Roberts et al. (2023, in prep.) to create a sample of subgiant from APOGEE DR17 (Majewski et al. 2017). apogee is part of the Sloan Digital Sky Survey and measures high-resolution spectra of thousands of stars (Abdurro'uf et al. 2022). Chemical abundances are determined from the APOGEE Stellar Parameter and Chemical Abundance Pipeline (ASPCAP) (García Pérez et al. 2016).

Photospheric C and N abundances in subgiant are reflective of their birth abundances (Gilroy 1989; Korn et al. 2007; Lind et al. 2008; Souto et al. 2018, 2019). As first dredge up, which affects C and N abundances, only occurs during the ascent onto the RGB, subgiant stars are unaffected by this enrichment.

An alternate approach for this analysis would be to estimate the birth abundances of RGB stars by correcting surface abundance effects from first dredge up as in Vincenzo et al. (2021). Subgiants are the more attractive option since these observations do not rely on model-dependent corrections. However, RGB stars are more luminous, potentially allowing better coverage of the Galactic disk.

We choose to use Roberts et al. (2023, in prep.) sample as this does not rely on additional layers of modeling, providing a more direct constraint to our model and limiting our systematic uncertainties.

Fig. 6 shows a plot of all APOGEE stars and the Roberts et al. (2023, in prep.) polygon selection criteria. Roberts et al. (2023, in prep.) select a region of stars based on surface gravity  $\log g$ , and effective surface temperature,  $T_{\text{eff}}$ .

$$\begin{cases} \log g \geq 3.5 \\ \log g \leq 0.004 T_{\text{eff}} - 15.7 \\ \log g \leq 0.000706 T_{\text{eff}} + 0.36 \\ \log g \leq -0.0015 T_{\text{eff}} + 12.05 \\ \log g \geq 0.0012 T_{\text{eff}} - 2.8. \end{cases} \quad (11)$$

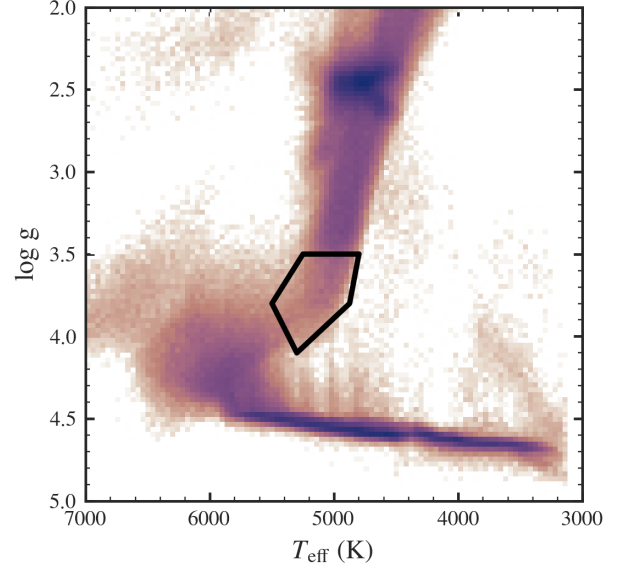


**Figure 6.** A Kiel diagram of APOGEE stars. Following Roberts et al. (2023, in prep.), we select subgiants in the black pentagon (see Equation 11). These stars have not yet experienced first dredge-up, so their photospheric C and N abundances should reflect their birth mixture.

Additionally, we included stars in APOGEE marked by the following flags.

```
APOGEE_MIRCLUSTER_STAR
APOGEE_EMISSION_STAR
APOGEE_EMBEDDEDCLUSTER_STAR
young cluster (IN-SYNC)
APOGEE2_W345
EB planet
```

This cut isolates a clean sample of  $\sim 12,000$  subgiants. We furthermore isolate the low- and high- $\alpha$  sequences with the cut

$$\begin{cases} [\text{Mg}/\text{Fe}] > 0.12 - 0.13 [\text{Fe}/\text{H}], & [\text{Fe}/\text{H}] < 0 \\ [\text{Mg}/\text{Fe}] > 0.12, & [\text{Fe}/\text{H}] > 0. \end{cases} \quad (12)$$

The low- $\alpha$  sequence is better reproduced by this model, so we use this cut of the subgiants to compare the models against except for comparing  $[\text{C}/\text{Mg}]$ - $[\text{Mg}/\text{Fe}]$ .

## 5 RESULTS

### 5.1 Evolution of Carbon Abundances

Here, we present the time evolution of our fiducial model. In the next sections, we will discuss the choice of parameters and agreement with observations. The fiducial model has the following qualitative characteristics of its C yields.

- C is mostly ( $\sim 80\%$ ) produced in CCSNe
- CCSNe produce more C at higher metallicities
- AGB stars produce less C at higher metallicities

The fiducial model uses the C11 AGB yield tables uniformly scaled by a factor of 2.9 (see Section 2.1, and Table 1).

Fig. 7 shows time evolution tracks of the fiducial model for  $[\text{C}/\text{Mg}]$ - $[\text{Mg}/\text{H}]$  and  $[\text{C}/\text{Mg}]$ - $[\text{Mg}/\text{Fe}]$ . As discussed in Section 2.3,  $[\text{C}/\text{Mg}]$ - $[\text{Mg}/\text{H}]$  is set by the total C/Mg yields.  $[\text{C}/\text{Mg}]$ - $[\text{Mg}/\text{Fe}]$  is instead

useful in understanding delayed C production. As both Fe and C are delayed elements, [Mg/Fe] steadily decreases after a star formation event, unlike [Mg/H] which quickly reaches equilibrium. All plots showing [C/Mg]-[Mg/Fe] going forward are selected in metallicity such that  $-0.15 \leq [\text{Mg}/\text{H}] \leq -0.05$ , so metallicity-dependent yields do not affect this plot. The [C/Mg]-[Mg/Fe]-diagram is, in essence, an empirical delay-time-distribution for a single stellar population of C, especially as we assume a  $\propto t^{-1.1}$  delay-time-distribution for Fe. Comparing the left and right panels of Fig. 7 highlights the differences between [C/Mg]-[Mg/H] and [C/Mg]-[Mg/Fe]. While [C/Mg]-[Mg/H] quickly reaches its final equilibrium distribution (within  $\sim 5$  Gyr), [C/Mg]-[Mg/Fe] continues to evolve in both [Mg/Fe] and [C/Mg] until the simulation ends.

C evolution proceeds as follows, (for a single zone)

- (i) CCSNe initially dominate production. As  $y_{\text{C}}^{\text{cc}}$  has strong metallicity dependence, [C/Mg] increases with time.
- (ii) AGB stars contribute delayed C, causing [C/Mg] to increase even faster with [Mg/H].
- (iii) [C/Mg] plateaus as C also approaches equilibrium.
- (iv) [C/Mg] may decrease due to declining SFH or slightly negative yields from  $\sim 1 M_{\odot}$  stars.

## 5.2 High-Mass Stellar Yields

CCSNe, which we assume make up the majority of C, set the overall C abundance trends. The top of Fig. 8 shows models with varying  $y_{\text{C}}^{\text{cc}}$  metallicity dependence,  $\zeta^{\text{cc}}$ . As the [C/Mg]-[Mg/H] trend is approximated by equilibrium trends, the models with higher  $\zeta^{\text{cc}}$  also have a steeper slope in [C/Mg]-[Mg/H]. However, [C/Mg]-[Mg/Fe] is minimally affected by changes to  $\zeta^{\text{cc}}$  since CCSNe occurs on much shorter timescales than SNe Ia and AGB enrichment. The only effects on [C/Mg]-[Mg/Fe], when considering the narrow metallicity slice, are because of either the slight change in equilibrium abundances, the imperfect evolution of the galaxy, or that the interstellar medium abundances are set by stars which were born at poorer metallicities. Hence, [C/Mg]-[Mg/H] tells us about the total C yield with metallicity, which [C/Mg]-[Mg/Fe] is independent of. If we know the AGB C yields, then with observed [C/Mg]-[Mg/Fe] abundance trends, we can infer the CCSNe C yields with metallicity.

## 5.3 Low-Mass Stellar Yields

To parameterize the AGB contribution to C production, we define  $f_{\text{agb}}$  to be the fraction of C which comes from AGB stars.

$$f_{\text{agb}} \equiv \frac{y_{\text{C}}^{\text{agb}}(Z = Z_{\odot})}{y_{\text{C}}(Z = Z_{\odot})}, \quad (13)$$

In Section 5.3, we will show that  $f_{\text{agb}} \approx 0.2$ . None of the AGB yield sets (C11, K10, V13, K16) produce enough C relative to our total  $y_{\text{C}}^{\text{cc}}$  values. So, we introduce a normalization factor  $\alpha_{\text{agb}}$ , which denotes a multiplicative scaling of  $y_{\text{C}}^{\text{agb}}$

$$y_{\text{C}}^{\text{agb}} \rightarrow \alpha_{\text{agb}} y_{\text{C}}^{\text{agb}}. \quad (14)$$

Table 2 contains the required values of  $\alpha_{\text{agb}}$  to reach  $f_{\text{agb}} = 0.2$ , the yields at solar metallicity, and the metallicity for each AGB yield set.

We can use the [C/Mg]-[Mg/Fe] diagram of APOGEE stars to estimate the delayed portion of C. When binned in metallicity, median [C/Mg] changes by about 0.2 dex across the range of [Mg/Fe] at solar metallicities. As high- $\alpha$  stars have little to no delayed SNe Ia Fe, these

stars would also have little to no delayed AGB C. This means that AGB C stars make up about at most a fraction  $f_{\text{agb}} \approx 1 - 10^{-0.2} \approx 0.4$  of C production.

[C/Mg]-[Mg/Fe] is sensitive to the assumptions about delayed C from AGB stars. If no C comes from low-mass stars, then [C/Mg] would be independent of [Mg/Fe], only [Mg/H]. Instead, C shows strong trends in [C/Mg]-[Mg/Fe] independent of metallicity.

In the middle row of Fig. 8, we first show the four C yield models (K10, K16, C11, V13). For the most part, the AGB yield sets result in qualitatively similar predictions. V13, however, does not reproduce solar trends as the model predicts strong C production at slightly above solar metallicities, resulting in a decreasing [C/Mg] with [Fe/Mg]. As all AGB models predict some low-mass C destruction, each model does predict a downturn in [C/Mg] as [Fe/Mg] increases. A recent burst in star formation may hide this downturn (see section 5.4), but the C destruction is not supported directly by observations.

We also investigate adjustments to the AGB yield fraction  $f_{\text{agb}}$ . The bottom of Fig. 8 shows three models with different AGB fractions while using C11 yields. The [C/Mg]-[Mg/Fe] relationship is set by  $f_{\text{agb}}$  because a specific amount of C must be released at a delayed time to match the SNe Ia production of Fe and increase [C/Mg] as [Mg/Fe] decreases to reproduce the data. Increased  $f_{\text{agb}}$  results in a decreased slope in [C/Mg]-[Mg/H], owing to the negative metallicity dependence of  $y_{\text{C}}^{\text{agb}}$ . So while [C/Mg]-[Mg/H] alone cannot differentiate models which vary  $f_{\text{agb}}$  and  $\zeta$  correspondingly, [C/Mg]-[Mg/Fe] provides information on  $f_{\text{agb}}$ . So, we can use [C/Mg]-[Mg/Fe] to estimate  $f_{\text{agb}} \approx 0.2$ , and then choose  $\zeta$  to match [C/Mg]-[Mg/H].

Finally, in the top row of Fig. 9, we plot FINISH where C production occurs in different mass ranges. If all C comes from stars with masses  $> 4M_{\odot}$ , then [C/Mg] is almost independent of [Fe/Mg]. On the other hand, if all C comes from stars with masses between 1 and  $2 M_{\odot}$ , then [C/Mg] increases across almost the whole range of [Fe/Mg]. As the observed trend in [C/Mg]-[Mg/Fe] is almost linear, then the delay-time-distribution of C is similar to Fe, so C is likely produced in a mix of stars between 1 and  $4M_{\odot}$ . We cannot constrain upper-intermediate AGB C production as this behaves similar to CCSNe C.

## 5.4 Star Formation History and Outflows

In this section, we consider two modifications of our fiducial SFH: *lateburst* and *earlyburst*. Our lateburst model adds a Gaussian factor to the inside-out SFH,

$$\dot{\Sigma}_{\text{lateburst}} \propto \dot{\Sigma}_{\text{inside-out}} \left( 1 + A e^{-(t - \tau_{\text{burst}})^2 / 2\sigma_{\text{burst}}^2} \right) \quad (15)$$

where  $A = 1.5$  represents the amplitude of the birth,  $\tau_{\text{burst}} = 10.8$  Gyr is the time where the burst is strongest, and  $\sigma_{\text{burst}} = 1$  Gyr is the width of the burst.

The middle row of Fig. 9 shows three models with our alternate SFH. Changes to the SFH leave [C/Mg]-[Mg/H] unchanged, but they do introduce slight variation in [C/Mg]-[Mg/Fe]. Models with higher AGB fractions are more sensitive to variations in the SFH. The late burst models result in [C/Mg] continuing to increase at low [Mg/Fe], but also introduce a dip not present in the data. Additionally, the early-burst reproduces the slight break between the low and high  $\alpha$  sequences, but overshoots equilibrium more severely than the fiducial model. In general, any of these SFHs are consistent with this model.

The middle row of Fig. 9 also shows a model where  $\eta$  and yields are decreased by a factor 0.3. While changing the value of  $\eta$  affects the metallicity distribution of stars, the model still evolves along the



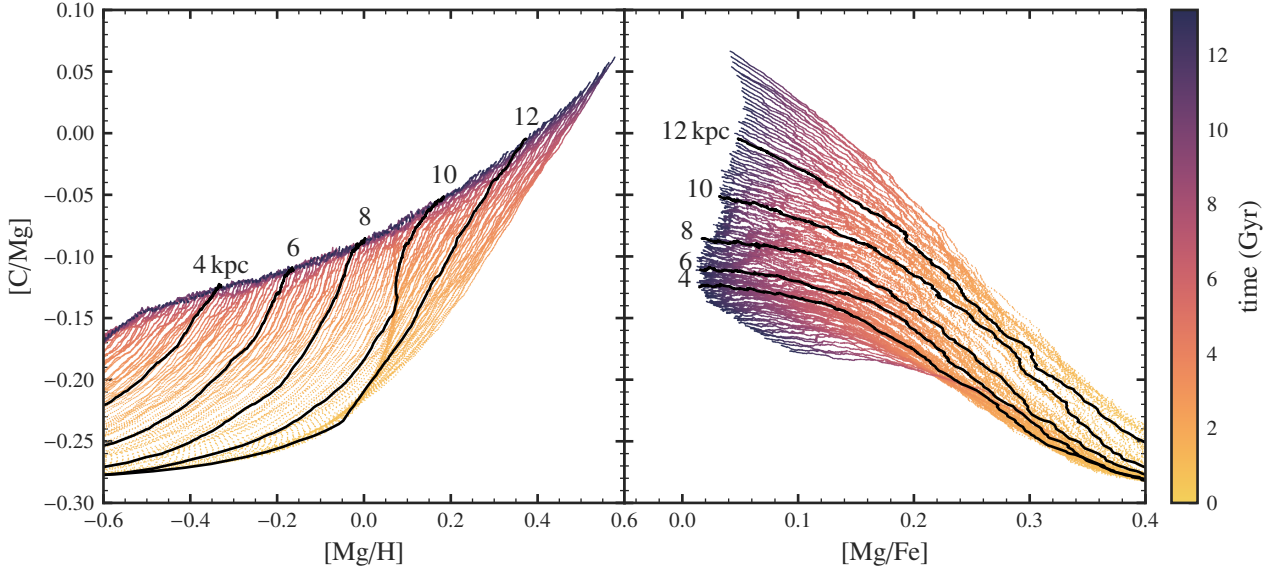


**Figure 7.** Time evolution of gas-phase C abundances in our fiducial model. Each line represents a zone at a different galactic radii. The lines are coloured-coded by time. The left shows  $[C/Mg]$ - $[Mg/H]$  and the right  $[C/Mg]$ - $[Mg/Fe]$ .

same paths. Our model is unable to differentiate a uniform decrease in both outflows and yields.

### 5.5 Degeneracies

Our conclusions are limited by the many uncertainties in GCE modeling.

The overall scaling of yields and outflows is unknown and challenging to constrain. GCE models of the Milky Way fall into two classes – those which incorporate significant mass-loading (e.g., this work) and those which neglect mass-loading but lower effective yield to match observed abundances (e.g. Minchev et al. 2013, 2014; Spitoni et al. 2019, 2020, 2021). An increase in stellar yields has a nearly identical effect as a decrease in the mass-loading factor  $\eta$  (see Appendix B of Johnson et al. 2022). The equilibrium arguments discussed in Section 2.3 suggest however that abundance ratios are independent of the choice of normalization and the value of  $\eta$ . We, therefore, expect our results regarding the relative yield  $y_C/y_{Mg}$  and its metallicity dependence to extend to the other class of models omitting mass loading. We demonstrate this further here. The theoretical motivation for decreasing yields is the uncertainty in stellar explodability. If fewer high-mass stars explode, then the yields will be reduced by some factor. Additionally, some fraction of supernovae ejecta may be lost directly to an outflow, lowering effective yields. To explore reduced outflow models, we lower both  $\eta$  and all yields by the same factor to leave the equilibrium abundances unchanged.

An addition source of theoretical uncertainty in this result is that the SNe Ia yield and delay time distributions have their own uncertainties. We do compute models (not shown here) where  $y_{Fe}^{Ia}$  is varied. Increasing  $y_{Fe}^{Ia}$  has a similar affect as decreasing  $f^{agb}$ . Here, we only show models with  $y_{Fe}^{Ia} = 0.00214$  and a  $t^{-1.1}$  delay-time-distribution choices from the fiducial model here.

### 5.6 Gas-Phase Abundances

As a final test of the model, we compare the model predictions against gas-phase measurements. Fig. 10 shows the fiducial model’s gas-phase predictions compared to observations of the Milky Way and extragalactic HII regions, halo stars, and damped Lyman-alpha systems. While observations in HII regions and Milky Way stars agree that C/O generally increases at near-solar metallicities, damped Lyman-alpha systems and metal poor stars imply that C/O may also increase again at very low metallicities.

Measurements of C abundances are challenging. In HII regions, C/O abundance ratios are measured with either recombination lines or collisional excitation lines. While broad consistency of our model with gas-phase measurements is promising, the large measurement errors limit the evaluative power of HII regions. We additionally include Milky Way thick disk (high- $\alpha$ ) and halo stars, which span a larger range of metallicities than thin disk stars. However, metal-poor abundance measurements require consideration of 3D-NLTE effects, which can be an  $\sim 0.2$  dex effect (e.g. CITE). Finally, dwarf galaxies, damped Lyman-alpha systems, and extragalactic regions may represent different SFHs than the Milky Way. As AGB C production is sensitive to variations in the SFH, these environments may not exactly match our subgiant sample, limiting the usefulness of these abundance measurements in evaluating our model.

C lines are relatively faint, and surveys such as GALAH struggle against low detection rates, potentially biasing sample measurements. (e.g. gaia-eso AS WELL Franchini et al. 2020). In the gas phase, HII regions are our best window into C abundances. Unfortunately, C lacks strong collisional excitation lines, and recombination lines fall in the ultraviolet without nearby reference H lines (Skillman et al. 2020). Recombination-line and collisional-excitation-line measurements furthermore disagree by a factor of  $\sim 2$  (García-Rojas & Esteban 2007).

Fig. 10 shows the single-zone model and time-slices of the fiducial multi-zone model at present day and  $t = 2$  Gyr. Here, we consider a single-zone model with parameters consistent with the Gaia-Encelidus sausage<sup>10</sup>. We chose the model to have mass loading

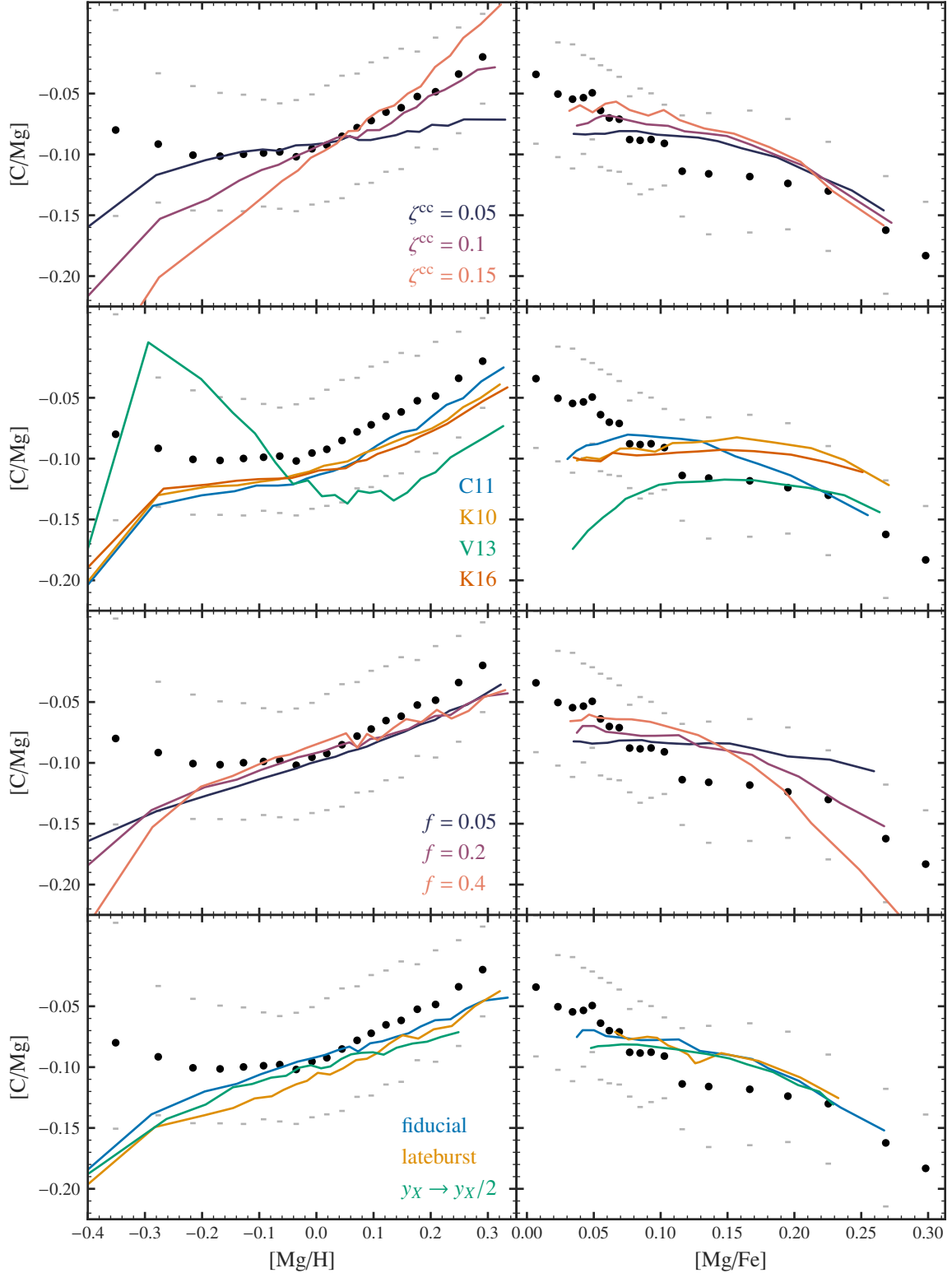


**Figure 8.** Stellar abundance trends in our model, assuming metallicity independent  $y_{\text{C}}^{\text{cc}}$ . Coloured lines represent the median  $[\text{C}/\text{Mg}]$  in bins of  $[\text{Mg}/\text{H}]$  (left) or  $[\text{Mg}/\text{Fe}]$  (right) for each model. Black points and grey dashes represent the median and standard deviations of  $[\text{C}/\text{Mg}]$  for each  $[\text{Mg}/\text{H}]$  bin in the Roberts et al. (2023, in prep.) sample. In the right panels, we show the trends only for stars where  $-0.15 \leq [\text{Mg}/\text{H}] \leq -0.05$ . **Top:** Models with different metallicity dependences for CCSNe C yields. **Middle:** Our four different AGB models. **Bottom:** Different AGB fractinos of C.

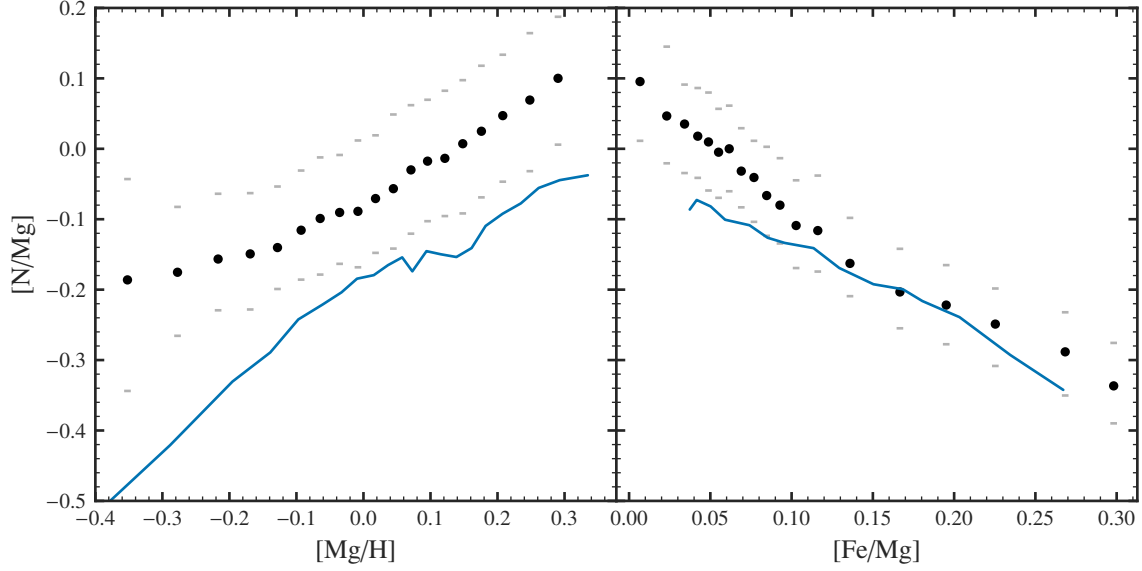


**Figure 9.** Similar to Fig. 8. The top panels show models with different mass-ranges contributing AGB C yields. The middle panels show different star formation histories (section 5.4) and yield normalizations. The bottom panels show  $[N/Mg]$  against  $[Mg/H]$  and  $[Fe/Mg]$  for the fiducial model.

$\eta = 20$ , star formation efficiency  $\tau_{\star} = 16$  Gyr, and a star formation history  $\propto e^{-t/3 \text{ Gyr}}$ , evolved for 2 Gyr (Johnson et al. 2022). The single-zone model is better able to replicate the slope of the abundances in dwarf galaxies, HII-regions, and halo stars. The single-zone model does not produce an equilibrium track, unlike the multi-zone models. As the single-zone model also evolves slower, the late contribution of AGB stars causes the steeper slope at near-solar metallicities. By including an increase of C yields at low-metallicity, the single-zone model is also able to reproduce the increasing  $[C/O]$  abundances with decreasing metallicity past  $[O/H] < -1.5$ . In any case, there is large scatter in the measurements, which both models fall within.

## 6 CONCLUSIONS

In this work, we investigated the role of C yields on the predictions of multi-zone GCE models. We began by adopting an equilibrium approximation to estimate the total C yields with metallicity from APOGEE subgiant  $[C/Mg]$ - $[Mg/H]$  trends. We find that  $y_C/y_O = 1/3 + 4(Z - Z_{\odot})$  and  $y_C/y_{Mg} = 2.7 + 32(Z - Z_{\odot})$ , where we assume  $[Mg/O] = 0$ . We show that  $[C/Mg]$ - $[Mg/H]$  is a diagnostic for total C yields with metallicity, but  $[C/Mg]$ - $[Mg/Fe]$  provides information about delayed C production. From the  $[C/Mg]$ - $[Mg/Fe]$  trends, we estimate that AGB stars with masses between about 1 and 3  $M_{\odot}$  contribute  $\sim 20\%$  of total C abundances. In this model, the remaining  $\sim 80\%$  of C comes from high-mass stars with a metallicity dependent yield of  $y_C^{\text{cc}}/y_{Mg} = 2.2 + 55(Z/Z_{\odot})$ , broadly consistent with rotating CCSNe models.

We additionally explore variations of the assumed SFH and outflow mass-loading factor  $\eta$ . We find that alternate SFHs can perturb

$[C/Mg]$ - $[Mg/Fe]$  and  $[C/Mg]$ - $[Mg/H]$  abundances slightly. Decreasing both outflows and yields by the same factor leaves the  $[C/Mg]$ - $[Mg/H]$  and  $[C/Mg]$ - $[Mg/Fe]$  trends unaffected, ignoring effect to the metallicity distribution of stars. These constraints on the relative yields of C, O, and Mg are robust against variations in  $\eta$ .

Finally, we compare our model against gas-phase measurements and Milky Way halo stars. By including yields which are enhanced at low metallicities, CCSNe and AGB stars together are able to explain the general trends of C from metallicities of  $[O/H] = -3$  to 0.5.

Our C yield constraints provide a useful benchmark for stellar evolution models. C yields are sensitive to poorly understood processes, including mass-loss prescriptions, explosibility, nuclear cross sections, convection, and stellar structure. Future spectroscopic surveys combined with Gaia kinematics (Gaia Collaboration et al. 2016) will continue to enhance our understanding of chemical evolution. Both the Sloan Digital Sky Survey V's Milky Way Mapper program (SDSS-V/MWM) (Kollmeier et al. 2017) and the Dark Energy Spectroscopic Instrument (DESI) Milky Way survey (DESI Collaboration et al. 2016; Cooper et al. 2022) will each measure spectra of upwards 6,000,000 Milky Way stars. These larger samples will enable similar work to tighten constraints on stellar models and our understanding of galaxy structure and evolution.

## ACKNOWLEDGEMENTS

Here you can thank helpful colleagues, acknowledge funding agencies, telescopes and facilities used etc. Try to keep it short.

Software that has contributed to this work included VICE (Johnson & Weinberg 2020; Johnson et al. 2021), MATPLOTLIB (Hunter 2007), SCIPY (Virtanen et al. 2020), IPYTHON (Pérez & Granger 2007), PANDAS (pandas development team 2020), NUMPY (Harris et al. 2020), ASTROPY (Astropy Collaboration et al. 2013, 2018, 2022), and SEABORN (Waskom 2021). Additionally, we thank Ohio Supercomputer Center (1987) for the use of its facilities for the simulations.

<sup>10</sup> See e.g. CITATION. The Gaia-Enceladus sausage (GSE) is a kinematically and chemically distinct group of halo stars consistent with the merger of a dwarf galaxy early in the Milky Way's formation.

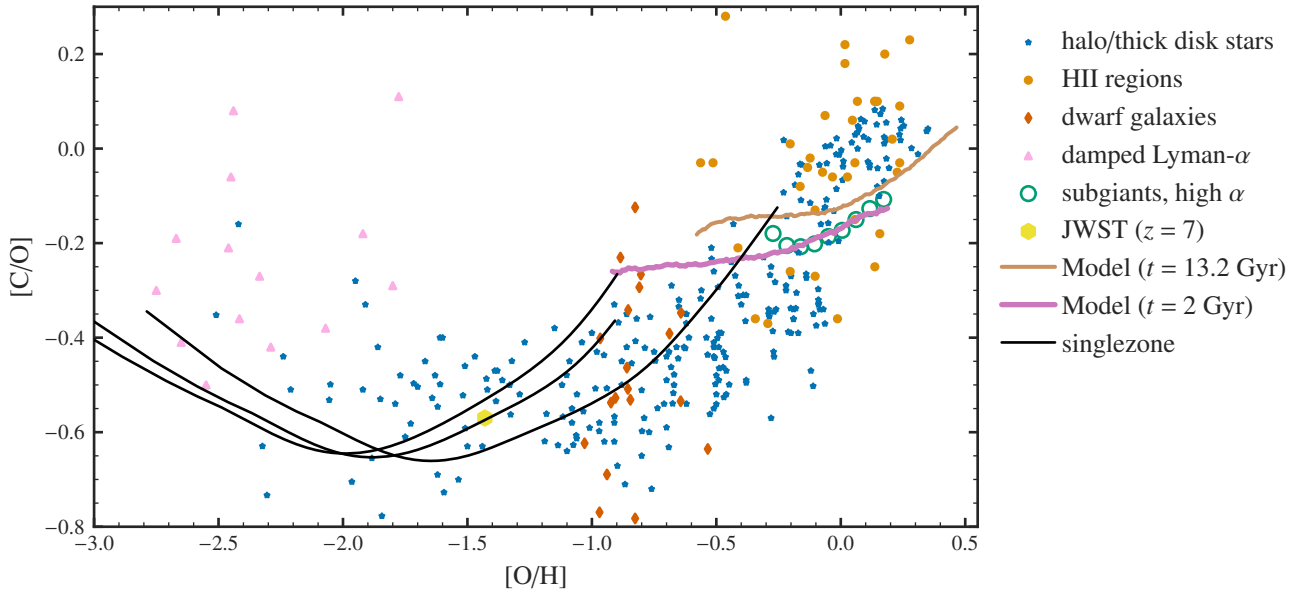


**Figure 10.** Gas-phase C abundances. We plot our model at  $t = 2$  Gyr and present day as thick solid lines. Black lines are single-zone models. Points represent measurements in HII regions (pink circles; Skillman et al. 2020; Esteban et al. 2002, 2009, 2014, 2019) damped Lyman-alpha (DLA) systems (blue triangles; Ellison et al. 2010; Srianand et al. 2010; Dutta et al. 2014; Dessauges-Zavadsky et al. 2003; Pettini et al. 2008; Morrison et al. 2016; Cooke et al. 2017), dwarf galaxies (red diamonds; Berg et al. 2019), Milky Way halo and thick disk stars (green stars; Amarsi et al. 2019; Nissen et al. 2014; Fabbian et al. 2009), and Milky Way high- $\alpha$  stars (yellow points; Robert et al. 2023, in prep.).

## DATA AVAILABILITY

The inclusion of a Data Availability Statement is a requirement for articles published in MNRAS. Data Availability Statements provide a standardised format for readers to understand the availability of data underlying the research results described in the article. The statement may refer to original data generated in the course of the study or to third-party data analysed in the article. The statement should describe and provide means of access, where possible, by linking to the data or providing the required accession numbers for the relevant databases or DOIs.

## REFERENCES

- Abdurro'uf et al., 2022, *ApJS*, **259**, 35  
 Adelberger E. G., et al., 2011, *Reviews of Modern Physics*, **83**, 195  
 Amarsi A. M., Nissen P. E., Skúladóttir Á., 2019, *A&A*, **630**, A104  
 Asplund M., Grevesse N., Sauval A. J., Scott P., 2009, *ARA&A*, **47**, 481  
 Astropy Collaboration et al., 2013, *A&A*, **558**, A33  
 Astropy Collaboration et al., 2018, *AJ*, **156**, 123  
 Astropy Collaboration et al., 2022, *ApJ*, **935**, 167  
 Bensby T., Feltzing S., 2006, *MNRAS*, **367**, 1181  
 Berg D. A., Erb D. K., Henry R. B. C., Skillman E. D., McQuinn K. B. W., 2019, *ApJ*, **874**, 93  
 Bird J. C., Kazantzidis S., Weinberg D. H., 2012, *MNRAS*, **420**, 913  
 Bird J. C., Kazantzidis S., Weinberg D. H., Guedes J., Callegari S., Mayer L., Madau P., 2013, *ApJ*, **773**, 43  
 Bird J. C., Loebman S. R., Weinberg D. H., Brooks A. M., Quinn T. R., Christensen C. R., 2021, *MNRAS*, **503**, 1815  
 Bland-Hawthorn J., Gerhard O., 2016, *ARA&A*, **54**, 529  
 Brooks A. M., Zolotov A., 2014, *ApJ*, **786**, 87  
 Chiappini C., Romano D., Matteucci F., 2003, *MNRAS*, **339**, 63  
 Christensen C., Quinn T., Governato F., Stilp A., Shen S., Wadsley J., 2012, *MNRAS*, **425**, 3058  
 Cooke R. J., Pettini M., Steidel C. C., 2017, *MNRAS*, **467**, 802  
 Cooper A. P., et al., 2022, *arXiv e-prints*, p. arXiv:2208.08514  
 Cristallo S., et al., 2011, *ApJS*, **197**, 17  
 Cristallo S., Straniero O., Piersanti L., Gobrecht D., 2015, *ApJS*, **219**, 40  
 DESI Collaboration et al., 2016, *arXiv e-prints*, p. arXiv:1611.00036  
 Dalcanton J. J., 2007, *ApJ*, **658**, 941  
 Dearborn D. S. P., Tinsley B. M., Schramm D. N., 1978, *ApJ*, **223**, 557  
 Dessauges-Zavadsky M., Péroux C., Kim T. S., D'Odorico S., McMahon R. G., 2003, *MNRAS*, **345**, 447  
 Dutta R., Srianand R., Rahmani H., Petitjean P., Noterdaeme P., Ledoux C., 2014, *MNRAS*, **440**, 307  
 Ellison S. L., Prochaska J. X., Hennawi J., Lopez S., Usher C., Wolfe A. M., Russell D. M., Benn C. R., 2010, *MNRAS*, **406**, 1435  
 Esteban C., Peimbert M., Torres-Peimbert S., Rodríguez M., 2002, *ApJ*, **581**, 241  
 Esteban C., Bresolin F., Peimbert M., García-Rojas J., Peimbert A., Mesa-Delgado A., 2009, *ApJ*, **700**, 654  
 Esteban C., García-Rojas J., Carigi L., Peimbert M., Bresolin F., López-Sánchez A. R., Mesa-Delgado A., 2014, *MNRAS*, **443**, 624  
 Esteban C., García-Rojas J., Arellano-Córdova K. Z., Méndez-Delgado J. E., 2019, *arXiv e-prints*, p. arXiv:1905.10129  
 Fabbian D., Nissen P. E., Asplund M., Pettini M., Akerman C., 2009, *A&A*, **500**, 1143  
 Finlator K., Davé R., 2008, *MNRAS*, **385**, 2181  
 Franchini M., et al., 2020, *ApJ*, **888**, 55  
 Frankel N., Rix H.-W., Ting Y.-S., Ness M., Hogg D. W., 2018, *ApJ*, **865**, 96  
 Frankel N., Sanders J., Ting Y.-S., Rix H.-W., 2020, *ApJ*, **896**, 15  
 Frinchaboy P. M., et al., 2013, *ApJ*, **777**, L1  
 Gaia Collaboration et al., 2016, *A&A*, **595**, A1  
 García Pérez A. E., et al., 2016, *AJ*, **151**, 144  
 García-Rojas J., Esteban C., 2007, *ApJ*, **670**, 457  
 Gilroy K. K., 1989, *ApJ*, **347**, 835  
 Griffith E. J., Sukhbold T., Weinberg D. H., Johnson J. A., Johnson J. W., Vincenzo F., 2021, *ApJ*, **921**, 73  
 Harris C. R., et al., 2020, *Nature*, **585**, 357  
 Hayden M. R., et al., 2014, *AJ*, **147**, 116  
 Henry R. B. C., Edmunds M. G., Köppen J., 2000, *ApJ*, **541**, 660  
 Hunter J. D., 2007, *Computing in Science & Engineering*, **9**, 90



- Iben Icko J., 1967, *ARA&A*, **5**, 571
- Isern J., 2019, *ApJ*, **878**, L11
- Johnson J. A., 2019, *Science*, **363**, 474
- Johnson J. W., Weinberg D. H., 2020, *MNRAS*, **498**, 1364
- Johnson J. W., et al., 2021, *MNRAS*, **508**, 4484
- Johnson J. W., et al., 2022, *arXiv e-prints*, p. [arXiv:2210.01816](https://arxiv.org/abs/2210.01816)
- Johnson J. W., Weinberg D. H., Vincenzo F., Bird J. C., Griffith E. J., 2023, *MNRAS*, **520**, 782
- Karakas A. I., 2010, *MNRAS*, **403**, 1413
- Karakas A. I., Lattanzio J. C., 2014, *Publ. Astron. Soc. Australia*, **31**, e030
- Karakas A. I., Lugaro M., 2016, *ApJ*, **825**, 26
- Karakas A. I., Lugaro M., Carlos M., Cseh B., Kamath D., García-Hernández D. A., 2018, *MNRAS*, **477**, 421
- Kennicutt Robert C. J., 1998, *ARA&A*, **36**, 189
- Kobayashi C., Karakas A. I., Lugaro M., 2020, *ApJ*, **900**, 179
- Kollmeier J. A., et al., 2017, *arXiv e-prints*, p. [arXiv:1711.03234](https://arxiv.org/abs/1711.03234)
- Korn A. J., Grundahl F., Richard O., Mashonkina L., Barklem P. S., Collet R., Gustafsson B., Piskunov N., 2007, *ApJ*, **671**, 402
- Kroupa P., 2001, *MNRAS*, **322**, 231
- Larson R. B., 1972, *Nature Physical Science*, **236**, 7
- Larson R. B., 1974, *MNRAS*, **166**, 585
- Licquia T. C., Newman J. A., 2015, *ApJ*, **806**, 96
- Lilly S. J., Carollo C. M., Pipino A., Renzini A., Peng Y., 2013, *ApJ*, **772**, 119
- Limongi M., Chieffi A., 2018, *ApJS*, **237**, 13
- Lind K., Korn A. J., Barklem P. S., Grundahl F., 2008, *A&A*, **490**, 777
- Loebman S. R., Ivezić Ž., Quinn T. R., Governato F., Brooks A. M., Christensen C. R., Jurić M., 2012, *ApJ*, **758**, L23
- Majewski S. R., et al., 2017, *AJ*, **154**, 94
- Maoz D., Mannucci F., Brandt T. D., 2012, *MNRAS*, **426**, 3282
- Matteucci F., 2021, *A&ARv*, **29**, 5
- Minchev I., Chiappini C., Martig M., 2013, *A&A*, **558**, A9
- Minchev I., Chiappini C., Martig M., 2014, *A&A*, **572**, A92
- Mor R., Robin A. C., Figueras F., Roca-Fàbrega S., Luri X., 2019, *A&A*, **624**, L1
- Morrison S., Kulkarni V. P., Som D., DeMarcy B., Quiret S., Péroux C., 2016, *ApJ*, **830**, 158
- Nissen P. E., Chen Y. Q., Carigi L., Schuster W. J., Zhao G., 2014, *A&A*, **568**, A25
- Nomoto K., Kobayashi C., Tominaga N., 2013, *ARA&A*, **51**, 457
- Ohio Supercomputer Center 1987, Ohio Supercomputer Center, <http://osc.edu/ark:/19495/f5s1ph73>
- Pagel B. E. J., 2009, *Nucleosynthesis and Chemical Evolution of Galaxies*, 2 edn. Cambridge University Press, doi:10.1017/CBO9780511812170
- Peeples M. S., Shankar F., 2011, *MNRAS*, **417**, 2962
- Pérez F., Granger B. E., 2007, *Computing in Science and Engineering*, **9**, 21
- Pettini M., Zych B. J., Steidel C. C., Chaffee F. H., 2008, *MNRAS*, **385**, 2011
- Prantzos N., Abia C., Limongi M., Chieffi A., Cristallo S., 2018, *MNRAS*, **476**, 3432
- Romano D., 2022, *A&ARv*, **30**, 7
- Romano D., Karakas A. I., Tosi M., Matteucci F., 2010, *A&A*, **522**, A32
- Rybicki J., Just A., Rix H.-W., 2017, *A&A*, **605**, A59
- Sánchez S. F., 2020, *ARA&A*, **58**, 99
- Sellwood J. A., Binney J. J., 2002, *MNRAS*, **336**, 785
- Skillman E. D., Berg D. A., Pogge R. W., Moustakas J., Rogers N. S. J., Croxall K. V., 2020, *ApJ*, **894**, 138
- Souto D., et al., 2018, *ApJ*, **857**, 14
- Souto D., et al., 2019, *ApJ*, **874**, 97
- Spitoni E., Silva Aguirre V., Matteucci F., Calura F., Grisoni V., 2019, *A&A*, **623**, A60
- Spitoni E., Verma K., Silva Aguirre V., Calura F., 2020, *A&A*, **635**, A58
- Spitoni E., et al., 2021, *A&A*, **647**, A73
- Srianand R., Gupta N., Petitjean P., Noterdaeme P., Ledoux C., 2010, *MNRAS*, **405**, 1888
- Sukhbold T., Ertl T., Woosley S. E., Brown J. M., Janka H. T., 2016, *ApJ*, **821**, 38
- Tacconi L. J., et al., 2018, *ApJ*, **853**, 179
- Tinsley B. M., 1979, *ApJ*, **229**, 1046
- Tinsley B. M., 1980, *Fundamentals Cosmic Phys.*, **5**, 287
- Ventura P., Di Criscienzo M., Carini R., D'Antona F., 2013, *MNRAS*, **431**, 3642
- Ventura P., Dell'Agli F., Schneider R., Di Criscienzo M., Rossi C., La Franca F., Gallerani S., Valiante R., 2014, *MNRAS*, **439**, 977
- Ventura P., Karakas A., Dell'Agli F., García-Hernández D. A., Guzman-Ramirez L., 2018, *MNRAS*, **475**, 2282
- Ventura P., Dell'Agli F., Lugaro M., Romano D., Tailo M., Yagüe A., 2020, *A&A*, **641**, A103
- Vincenzo F., et al., 2021, *arXiv e-prints*, p. [arXiv:2106.03912](https://arxiv.org/abs/2106.03912)
- Virtanen P., et al., 2020, *Nature Methods*, **17**, 261
- Waskom M. L., 2021, *Journal of Open Source Software*, **6**, 3021
- Weinberg D. H., Andrews B. H., Freudenburg J., 2017, *ApJ*, **837**, 183
- Weinberg D. H., et al., 2019, *ApJ*, **874**, 102
- Weinberg D. H., et al., 2022, *ApJS*, **260**, 32
- Woosley S. E., Weaver T. A., 1995, *ApJS*, **101**, 181
- Zolotov A., et al., 2012, *ApJ*, **761**, 71
- pandas development team T., 2020, *pandas-dev/pandas: Pandas*, doi:10.5281/zenodo.3509134, <https://doi.org/10.5281/zenodo.3509134>

This paper has been typeset from a  $\text{\LaTeX}$  file prepared by the author.